View metadata, citation and similar papers at core.ac.uk
brought to you by CORE
provided by CERN Document Server

Cranked Skyrme-Hartree-Fock calculation for superdeformed and hyperdeformed rotational bands in N=Z nuclei from ^{32}S to ^{48}Cr

T. Inakura[a], S. Mizutori[b], M. Yamagami[a,c] and K. Matsuyanagi[a]

[a] *Department of Physics, Graduate School of Science, Kyoto University, Kitashirakawa, Kyoto 606-8502, Japan*

[b] *Department of Human Science, Kansai Women's College, Kashiwara City, Osaka 582-0026, Japan*

[c] *Institut de Physique Nucléaire, IN$_2$P$_3$-CNRS, 91406 Orsay Cedex, France*

Abstract

With the use of the symmetry-unrestricted cranked Skyrme-Hartree-Fock method in the three-dimensional coordinate-mesh representation, we have carried out a systematic theoretical search for the superdeformed and hyperdeformed rotational bands in the mass A=30-50 region. Along the N=Z line, we have found superdeformed solutions in ^{32}S, ^{36}Ar, ^{40}Ca, ^{44}Ti, and hyperdeformed solutions in ^{36}Ar, ^{40}Ca, ^{44}Ti, ^{48}Cr. The superdeformed band in ^{40}Ca is found to be extremely soft against both the axially symmteric (Y_{30}) and asymmetric (Y_{31}) octupole deformations. An interesting role of symmetry breaking in the mean field is pointed out.

PACS: 21.60-n; 21.60.Jz; 27.30.+t

Keywords: Cranked Skyrme-Hartree-Fock method; Superdeformation; Hyperdeformation; Non-axial octupole deformation; High-spin state; Calcium 40

1 Introduction

Nowadays, about two hundreds superdeformed (SD) rotational bands are identified in various mass (A=60, 80, 130, 150, 190) regions [1–6]. Every regions of superdeformation have their own characteristics so that we can significantly enlarge and deepen our understanding of nuclear structure by systematically investigating similarities and differences among the SD bands in different mass region. For the mass A=30-50 region, although the doubly magic SD band in ^{32}S, which has been expected quite a long time [7–15], has not yet been observed and remains as a great challenge [6], quite recently, beautiful rotational spectra associated with the SD bands have been observed up to high spin in neighboring N=Z nuclei; ^{36}Ar, ^{40}Ca, and ^{44}Ti. In ^{36}Ar the SD band has been identified up to its termination at $I^\pi = 16^+$ [16–18]. The SD band in the spherical magic nucleus ^{40}Ca is built on the well known 8p-8h excited 0^+ states at 5.213 MeV and the rotational spectra have been observed up to $I^\pi = 16^+$ [19]. In ^{44}Ti a rotational spectrum associated with the excited 0^+ state at 1.905 MeV has been observed up to $I^\pi = 12^+$ [20]. This rotational band may also be regarded as belonging to a family of the SD band configurations. The fact that rotational bands built on excited 0^+ states are systematically observed is a quite important, unique feature of the SD bands in the ^{40}Ca region, as the low angular momentum portions of the SD bands in heavier mass regions are unknown in almost all cases.

In nuclei along the N=Z line, effects of deformed shell structures of protons and neutrons act coherently and rich possibilities arise for coexistence and competition of different shapes. Thus, we shall be able to learn details of deformed shell structure and microscopic mechanism of shape coexistence by a systematic study of high-spin yrast structure in the sequence of N=Z nuclei. Especially, yrast spectroscopy of nuclei in the A=30-50 region, being relatively light compared to other regions of SD nuclei, is expected to provide detailed information about the roles of individual deformed single-particle orbits responsible for the emergence of the SD bands.

In this paper, as a continuation of the previous work on ^{32}S [21], we carry out a systematic theoretical search for SD and more elongated hyperdeformed (HD) rotational bands in N=Z nuclei from ^{32}S to ^{48}Cr by means of the symmetry-unrestricted, cranked Skyrme-Hartree-Fock (SHF) method. In Ref. [21], a new computer code was constructed for the cranked SHF calculation based on the three-dimensional (3D) Cartesian-mesh representation, which provides a powerful tool for exploring exotic shapes (breaking both axial and reflection symmetries in the intrinsic states) at high spin. The algorithm of this code for numerical calculation is basically the same as in Refs. [22–31], except that various restrictions on spatial symmetries are completely removed. Namely, we do not impose parity and signature symmetries on intrinsic wave functions. Hence we call this version of the cranked SHF method "symmetry-unrestricted" one. For the development of selfconsistent mean-field models for nuclear structure, we quote Refs. [2], [32] and [33], in which various kinds of

mean-field theory, including Hartree-Fock (HF) calculations with finite-range Gogny interactions [34] and relativistic mean-field approaches [35], are thoroughly reviewd. We also mention that spontaneous symmetry breaking in rotating nuclei is reviewd in [36].

In fact, SD and HD solutions of the SHF equations we report in this paper preserve the reflection symmetries with respect to the (x, y), (y, z) and (z, x) planes, so that the symmetry-unrestricted calculation gives identical results with those evaluated by imposing such symmtries. The symmetry-unrestricted calculation, however, enables us to examine stabilities of the SD and HD states against such reflection-symmetry breaking degrees of freedom like octupole deformations. In addition, we shall show that the symmetry breaking play a quite interesting role in the crossing region between different configurations away from the local minima in the deformation parameter space.

This paper is arranged as follows: In Section 2, a brief account of the cranked SHF method is given. In Section 3, results of calculation for deformation energy curves and the SD and HD rotational bands in nuclei from ^{32}S to ^{48}Cr are systematically presented. Here, special attention will be paied to the properties of the SD bands at their high spin limits and the crossover to the HD bands with increasing angular momentum. In Section 4, an interesting role of symmetry breaking in the mean field will be pointed out in connection with configuration rearrangement mechanism. We shall further make a detailed analysis of the SD band of ^{40}Ca and show that it is extremely soft against both the axially symmteric (Y_{30}) and asymmetric (Y_{31}) octupole deformations. Main results of this paper are summarized in Section 5.

A preliminary version of this work was reported in [37, 38].

2 Cranked SHF calculation

The cranked HF equation for a system uniformly rotating about the x-axis is given by

$$\delta < H - \omega_{\rm rot} J_x >= 0, \tag{1}$$

where $\omega_{\rm rot}$ and J_x mean the rotational frequency and the x-component of angular momentum, and the bracket denotes the expectation value with respect to a Slater determinantal state. We solve the cranked HF equation for a Hamiltonian of the Skyrme type by means of the imaginary-time evolution technique [22] in the 3D Cartesian-mesh representation. We adopt the standard algorithm [22, 25–27] in the numerical calculation, but completely remove various restrictions on spatial symmetries.

When we allow for the simultaneous breaking of both reflection and axial symmetries, it is crucial to accurately fulfill the center-of-mass condition

$$< \sum_{i=1}^{A} x_i >=< \sum_{i=1}^{A} y_i >=< \sum_{i=1}^{A} z_i >= 0, \tag{2}$$

and the principal-axis condition

$$< \sum_{i=1}^{A} x_i y_i >=< \sum_{i=1}^{A} y_i z_i >=< \sum_{i=1}^{A} z_i x_i >= 0. \tag{3}$$

For this purpose we use the constrained HF procedure with quadratic constraints [39]. Thus, we replace the "Routhian" $R = H - \omega_{\rm rot} J_x$ in Eq. (1) with

$$R' = R - \sum_{k=1}^{3} \mu_k < \sum_{i=1}^{A} (x_k)_i >^2 - \sum_{k<k'}^{3} \mu_{k,k'} < \sum_{i=1}^{A} (x_k x_{k'})_i >^2 . \tag{4}$$

In numerical calculations, we confirmed that the constraints (2) and (3) are fulfilled to the order $O(10^{-15})$ with values of the parameters $\mu_k \sim O(10^2)$ and $\mu_{k,k'} \sim O(1)$. We solved these equations inside the sphere with radius R=10 fm and mesh size h=1 fm, starting with various initial configurations. We note that the accuracy for evaluating deformation energies with this mesh size was carefully checked by Tajima *et al.* [27,28] (see also Ref. [40]) and was found to be quite satisfactory. The 9-point formula was used as the difference formula for the Laplacian operator. As usual, the angular momentum is evaluated as $I\hbar =< J_x >$. For the Skyrme interaction, we adopt the widely used three versions; SIII [41], SkM* [42] and SLy4 [43].

In addition to the symmetry-unrestricted cranked SHF calculation explained above, we also carry out, for comparison sake, symmetry-restricted calculations imposing reflection symmetries about the (x, y)-, (y, z)- and (z, x)-planes. The computational algorithm for this restricted version of the cranked SHF calculation is basically the same as in [26], but we have constructed a new computer code for this purpose. Below we call these symmetry-unrestricted and -restricted cranked SHF versions "unrestricted" and "restricted" ones, respectively. Comparison between results obtained by unrestricted and restricted calculations carried out independently serves as a check of numerical results to be presented below. Physical significance of this comparison is, however, that we can, in this way, clearly identify effects of symmetry-breaking in the mean field. We shall indeed find an interesting symmetry breaking effect in the next section.

Solutions of the cranked SHF equation give minima in the deformation energy surface. In order to explore the deformation energy surface around these minima and draw deformation energy curves as functions of deformation parameters, we carry out the constrained HF procedure with quadratic constraints [39]. Namely, in addition to the constraints to fulfil the center-of mass and principal-axis conditions mentioned above, we also introduce constraints involving relevant mass-multipole moment operators and solve resulting constrained HF equations.

As measures of the deformation, we calculate the mass-multipole moments,

$$\alpha_{lm} = \frac{4\pi}{3A\bar{R}^l} \int r^l X_{lm}(\Omega)\, \rho(\boldsymbol{r})\, d\boldsymbol{r}, \quad (m = -l, \cdots, l) \tag{5}$$

where $\rho(\boldsymbol{r})$ is the density, $\bar{R} = \sqrt{5 < \sum_{i=1}^{A} \boldsymbol{r}_i^2 > /3A}$, and X_{lm} are real bases of the spherical harmonics,

$$X_{l0} = Y_{l0}, \tag{6}$$

$$X_{l|m|} = \frac{1}{\sqrt{2}}(Y_{l-|m|} + Y^*_{l-|m|}), \tag{7}$$

$$X_{l-|m|} = \frac{-i}{\sqrt{2}}(Y_{l|m|} - Y^*_{l|m|}). \tag{8}$$

Here the quantization axis is chosen as the largest (smallest) principal axis for prolate (oblate) solutions. We then define the quadrupole deformation parameter β_2, the triaxial deformation parameter γ, and the octupole deformation parameters β_3 and β_{3m} by

$$\alpha_{20} = \beta_2 \cos\gamma, \quad \alpha_{22} = \beta_2 \sin\gamma, \tag{9}$$

$$\beta_3 = \left(\sum_{m=-3}^{3} \alpha_{3m}^2 \right)^{1/2}, \quad \beta_{3m} = \left(\alpha_{3m}^2 + \alpha_{3-m}^2 \right)^{1/2} \quad (m = 0, 1, 2, 3)\,. \tag{10}$$

For convenience, we also use the familiar notation $-\beta_2$ for oblate shapes with $(\beta_2, \gamma = 60^\circ)$.

3 Results of calculation

3.1 *Deformation energy curves*

Figures 1-3 show deformation energy curves evaluated at $I = 0$ by means of the constrained HF procedure with the quadratic constraint on the mass-quadrupole moment. The SIII, SkM*, and SLy4 versions of the Skyrme interaction are used in Figs. 1, 2, and 3, respectively. Solid lines with and without filled circles in these figures represent results of unrestricted and restricted calculations, respectively. Let us focus our attention to the region of large quadrupole deformation β_2. In both cases, we otain local minima corresponding to the SD states for ^{32}S, ^{36}Ar, ^{40}Ca and ^{44}Ti in the region $0.4 \leq \beta_2 \leq 0.8$. (The local minimum in ^{44}Ti is triaxial, as shown in Fig. 10 below, i.e., it is situated away from the $\gamma = 0$ section of the deformation energy surface, so that it is not clearly seen in Figs. 1-3.) The local minima in ^{32}S and ^{36}Ar involve four particles (two protons and two neutrons) in the fp shell, while those in ^{40}Ca and ^{44}Ti involve eight particles (four protons and four neutrons). These local minima respectively correspond to the 4p-12h, 4p-8h, 8p-8h and 8p-4h configurations with respect to the doubly closed shell of ^{40}Ca, and their properties have been discussed from various point of view;

see Refs. [7–15] for ^{32}S, Refs. [16–18, 44] for ^{36}Ar, Refs. [19, 45–51] for ^{40}Ca, and Refs. [20, 52, 53] for ^{44}Ti.

In addition to these SD minima, we also obtain local minima in the region $\beta_2 \geq 0.8$ for ^{40}Ca, ^{44}Ti and ^{48}Cr. These minima involve additional four particles (two protons and two neutrons) in the single-particle levels that reduces to the $g_{9/2}$ levels in the spherical limit. Somewhat loosely we call these local minima "hyperdeformed." The HD solution in ^{40}Ca corresponds to the 12p-12h configuration. For ^{44}Ti, we obtain two HD solutions which correspond to the 12p-8h and 16p-12h configurations. The HD solution in ^{48}Cr corresponds to the 16p-8h configuration. These HD solutions well agree with those previously obtained in the SHF calculation by Zheng, Zamick and Berdichevsky [49]. We also mention that the 12p-12h configuration in ^{40}Ca and the 16p-12h configuration in ^{44}Ti agree with those obtained by the macroscopic-microscopic model calculation by Leander and Larsson [8].

In Figs. 1-3 and in the following, the above SD and HD configurations are denoted by $f^n g^m$ (or $(fp)^n g^m$), where n and m indicate the numbers of nucleons occupying the $f_{7/2}$ shell (or the fp shell) and the $g_{9/2}$ shell, respectively.

As seen in Figs. 1-3, these SD and HD minima are obtained for all calculations with the use of the SIII, SkM*, and SLy4 interactions. These local minima preserve the reflection symmetries so that the results of restricted and unrestricted calculations are the same. On the other hand, we also find a case where the two calculations give different results: We obtain a HD minimum with $\beta_2 \simeq 0.8$ for ^{36}Ar in the restricted calculations. This minimum involves eight particles (four protons and four neutrons) in the fp shell and correspond to the 8p-12h configuration, but it disappears in the unrestricted calculations and its remnant remains as a shoulder of the deformation energy curve.

Although the restricted and unrestricted calculations give identical results for the SD and HD local minima except for the HD solution for ^{36}Ar, they show different behaviors in regions away from the local minima: In Figs. 1-3, we see that the deformation energy curves obtained by the unrestricted calculations always join different local minima smoothly. On the other hand, in the restricted calculations, segments of the deformation energy curves associated with different local minima sharply cross each other in some situations, while they are smoothly joined in other situations. Closely examining the configurations involved, we notice that the sharp crossings occur between configurations having different numbers of particles excited into the fp shell. This point will be further elaborated in the subsequent section.

In Figs. 1-3 there are a number of local minima in the region of smaller values of β_2. We shall not discuss on these local minima in this paper, since the pairing correlations not taken into account here are expected to be important for these.

The single-particle level schemes at the SD and HD local minima mentioned above are displayed in Figs. 4-6 at positions of their quadrupole deformation parameters β_2. One may notice that these equilibrium deformations correspond to values of β_2 slightly smaller than those where the amount of

energy spacings between the highest occupied and lowest unoccupied single-particles levels become local maxima. This is a characteristic common to three versions of the Skyrme interactions used, and in accord with the expectation that equilibrium deformations are determined by the sum of microscopic (shell-structure) and macroscopic (liquid-drop) energies; the latter shifts the equilibrium values of β_2 to slightly smaller ones.

3.2 *SD and HD rotational bands*

Let us focus our attention to the SD and HD local minima shown in Figs. 1-3, and investigate properties of the rotational bands built on them. Figures 7-9 show excitation energies, as functions of angular momentum, of the SD and HD rotational bands calculated with the use of the SIII, SkM*, and SLy4 interactions, respectively. These rotational bands are obtained by cranking each SHF solution (the SD and HD local minima in Figs. 1-3) and following the same configuration with increasing value of $\omega_{\rm rot}$ until the point where we cannot clearly identify the continuation of the same configuration any more. We note that, in ^{44}Ti, two HD bands associated with the f^8g^4 and $(fp)^{12}g^4$ configurations cross at $I = 30-34$, and the latter becomes the yrast for higher spin. (This band continues beyond $I = 40$ where the figure is cut.) In addition to the SD and HD bands built on the $I^\pi = 0^+$ band-head states, we have found a HD band in ^{36}Ar, which does not exist at $I = 0$ and emerges at $I \simeq 16$ due to the rotation alignment of the $g_{9/2}$ orbit. This HD band is denoted by f^6g^2 and is included in Figs. 7-9. A similar configuration, f^4g^2, was found for ^{32}S in our previous calculation [21] and called "HD-like." This and analogous configurations in nuclei other than ^{36}Ar are not illustrated in Figs. 7-9 in order not to make the figure too complicated (drawing complete yrast spectra of individual nuclei is not the major purpose of these figures).

As is well known, according to the deformed harmonic-oscillator potential model, $N = Z = 18$ and 24 are magic numbers associated with the HD shell structure with axis ratio 3 : 1. These HD states respectively correspond to the f^4g^4 and $f^{12}g^4h^4$ configurations in our notation, where h denotes the level associated with the $h_{11/2}$ shell. Microscopic structures of the HD solutions under discussion are apparently different from these, however. We also mention that the possible existence of HD rotational bands at high spin in ^{36}Ar and ^{48}Cr have been discussed in Refs. [54, 55] from the viewpoint of the cranked cluster model. The relationship between our solutions and their solutions associated with cluster structure is not clear.

Calculated quadrupole deformation parameters (β_2, γ) of all bands mentioned above and their variations are displayed in Fig. 10. The rotational frequency dependence of the single-particle energy levels (Routhian) is illustrated in Fig. 11, taking the SD band in ^{40}Ca as a representative case. The excitation energies of the SD and HD bands obtained by using different versions (SIII, SkM*, SLy4) of the Skyrme interaction are compared in Fig. 12 with the experimental data [16, 19, 20].

Examining these figures, we see that, aside from quantitative details and some subtle points to be discussed below, the results obtained by using different versions of the Skyrme interaction are similar. This implies that the basic properties of the SD and HD bands under discussion are not sensitive to the details of the effective interaction.

As mentioned in the introduction, one of the unique features of the SD bands in the ^{40}Ca region is the possibility to observe the SD rotational level structure from the $I^\pi = 0^+$ band heads up to the maximum angular momenta allowed for the many-particle-many-hole configurations characterizing the internal structures of these bands. In fact, such a "SD band termination" has been observed at $I = 16$ in ^{36}Ar and well described by calculations in terms of the j-j coupling shell model, the cranked Nilsson-Strutinsky model [16–18], and the projected shell model [44]. On the other hand, for ^{40}Ca and ^{44}Ti, it is not clear whether or not the SD band continues beyond the highest spin states observed up to now (the 16^+ state in ^{40}Ca [19] and the 12^+ state in ^{44}Ti [20]) and, quite recently, their properties, from the 0^+ band-heads to such high-spin regions, have been discussed in terms of the spherical shell model in Ref. [51] for ^{40}Ca and in Ref. [20] for ^{44}Ti. In our calculation, except for the case of using the SLy4 interaction, the band termination phenomenon in ^{36}Ar is reproduced; the shape becomes triaxial and evolves toward the oblate shape, although the oblate limit is not reached. In the cases of ^{40}Ca, the shape is slightly triaxial with $\gamma = 6°$-$9°(8°$-$9°)$ and the SD band terminates at $I \simeq 24$ in the calculation with the use of the SIII (SkM*) interaction. In the case of ^{44}Ti, the shape is more triaxial with $\gamma = 18°$-$25°$ and $13°$-$19°$, and the SD bands terminates at $I \simeq 12$ and 16 for the SIII and SkM* interactions, respectively. Thus, the band termination properties appear quite sensitive to the details of the effective interaction. Concerning the SD band termination in ^{40}Ca and ^{44}Ti, the results obtained with the use of the SIII and SkM* interactions would be more reliable than that with SLy4, in view of the above discussion for ^{36}Ar. In any case, it would be very interesting to explore higher spin members of the SD rotational bands in ^{40}Ca and ^{44}Ti in order to understand the terminating properties of the SD bands at high spin limits.

As is clear from the comparison with experimental data in Fig. 12, the moments of inertia for the SD band are somewhat overestimated in the present calculation. To investigate a possible cause of this, we plan to take into account the pairing correlations by means of the cranked Skyrme-Hartree-Fock-Bogoliubov code constructed in Ref. [56]. One also notice that the excitation energy of the SD band-head state in ^{40}Ca is overestimated. It will decrease if the zero-point rotational energy correction, $-\frac{1}{2\mathcal{J}} < J_x^2 >$, is taken into account(see Ref. [49] for numerical examples). Although the calculation of this correction is rather easy, we need to evaluate, for consistency, also the zero-point vibrational energy corrections [32], and this is not an easy task. We therefore defer this task for a future publication. Inclusion of these correlations is expected to improve agreement with the experimental data.

4 Discussions

4.1 *A role of symmetry breaking*

Let us now discuss on the significance of the reflection symmetry breaking in the mean field. As noticed in Figs. 1-3, the crossings between configurations involving different numbers of particles in the fp shell are sharp in the restricted calculation, while we always obtain smooth configuration rearrangements in the unrestricted calculations. The reason for this different behavior between the unrestricted and restricted calculations is rather easy to understand: When the parity symmetry is imposed, there is no way, within the mean-field approximation, to mix configurations having different number of particles in the fp shell. In contrast, smooth crossover between these different configurations is possible via mixing between positive- and negative-parity single-particle levels, when such a symmetry restriction is removed. Let us examine this idea in more detail. In Figs. 13-15 octupole deformation parameters β_3 of the lowest energy states for given values of β_2 are shown. They are obtained by the unrestricted SHF calculations and plotted as functions of β_2 in the lower portion of each panel. We see that β_3 are zero near the local minima in the deformation energy surface, but rise in the crossing region between configurations involving different number of particles in the fp shell. This means that the configuration rearrangements in fact take place through paths in the deformation space that break the reflection symmetry. The importance of allowing the mean field for breaking symmetries in the process of configuration rearrangements was previously emphasized by Negele [57] in their calculations for spontaneous fission of ^{32}S by means of the imaginary time tunneling method.

In connection with the above finding, it may be appropriate to point out another situation in which a symmetry breaking in the mean field plays an important role. For both the restricted and unrestricted calculations, we have obtained smooth crossover between the SD and HD configurations in ^{40}Ca and ^{44}Ti (see Figs. 1-3). Since four particles are further excited into the g shell in the HD configurations, the smooth configuration rearrangement becomes possible by means of the mixing between the down-sloping levels steming from the $g_{9/2}$ shell (its asymptotic quantum number is $[440]\frac{1}{2}$) and the up-sloping levels stemming from the sd shell ($[202]\frac{5}{2}$ and $[200]\frac{1}{2}$ in the cases of ^{40}Ca and ^{44}Ti, respectively). The mixing between these single-particle levels takes place through the hexadecapole components of the mean field, and we need to break the axial symmetry to mix them in the case of ^{40}Ca. The calculations called "restricted" in this paper allow the axial symmetry breaking, so that the smooth rearrangement from the SD to HD configurations is possible also in ^{40}Ca. A very careful computation is required, however, in order to detect these mixing effects, since the interaction between the down-sloping and up-sloping levels is extremely weak.

In Figs. 13-15, one may notice that β_3 take non-zero values also in some situations other than the crossing regions. Such situations occur in some regions

of the deformation energy surface where it becomes very soft with respect to the reflection-asymmetric degrees of freedom. In the next subsection, we investigate this point in detail taking the SD solution in ^{40}Ca as an especially interesting example.

4.2 *Octupole softness of the SD band in ^{40}Ca*

Let us examine stabilities of the SD local minimum in ^{40}Ca against octupole deformations. Figure 16 shows deformation energy curves as functions of the octupole deformation parameters $\beta_{3m}(m = 0, 1, 2, 3)$ for fixed quadrupole deformation parameters at and near the SD minimum of ^{40}Ca, calculated by means of the constrained HF procedure with the use of the SIII, SkM*, and SLy4 interactions. We immediately notice that the SD state is extremely soft with respect to the β_{30} and β_{31} deformations, irrespective of the Skyrme interactions used. Although it is barely stable with respect to these directions (see curves for $\beta_2 = 0.6$), an instability toward the β_{31} deformation occurs as soon as one goes away from the local minimum point (see curves for $\beta_2 = 0.5$). In fact, the deformation energy surface is found to be almost flat for a combination of the β_{30} and β_{31} deformations already at the SD local minimum. Thus we need to take into account the octupole shape fluctuations for a better description of the SD rotational band in ^{40}Ca. It will be a very interesting subject to search for negative-parity rotational bands associated with octupole shape fluctuation modes built on the SD yrast band. We plan to make such a study in future. Quite recently, the octupole instability of the SD band in ^{40}Ca has been suggested also by Kanada-En'yo [50].

5 Conclusions

With the use of the symmetry-unrestricted cranked SHF method in the 3D coordinate-mesh representation, we have carried out a systematic theoretical search for the SD and HD rotational bands in the N=Z nuclei from ^{32}S to ^{48}Cr. We have found the SD solutions in ^{32}S, ^{36}Ar, ^{40}Ca, ^{44}Ti, the HD solutions in ^{36}Ar, ^{40}Ca, ^{44}Ti, ^{48}Cr, and we have carried out a systematic analysis of their properties at high spin.

It is explicitly shown that the crossover between configurations involving different number of particles in the fp shell takes place via a reflection-symmery breaking path in the deformation space.

Particular attention has been paid to the recently discovered SD band in ^{40}Ca, and we have found that the SD band in ^{40}Ca is extremely soft against both the axially symmetric (Y_{30}) and asymmetric (Y_{31}) octupole deformations. Thus, it will be very interesting to search for negative-parity rotational bands associated with octupole shape vibrational excitations built on the SD yrast band.

Acknowledgements

We would like to thank E. Ideguchi, M. Matsuo, Y.R. Shimizu and K. Hagino for useful discussions. The numerical calculations were performed on the NEC SX-5 supercomputers at RCNP, Osaka University, and at Yukawa Institute for Theoretical Physics, Kyoto University. This work was supported by the Grant-in-Aid for Scientific Research (No. 13640281) from the Japan Society for the Promotion of Science.

References

[1] P.J. Nolan and P.J. Twin, Annu. Rev. Nucl. Part. Sci. 38 (1988) 533.

[2] S. Åberg, H. Flocard and W. Nazarewicz, Annu. Rev. Nucl. Part. Sci. 40 (1990) 439.

[3] R.V.F. Janssens and T.L. Khoo, Annu. Rev. Nucl. Part. Sci. 41 (1991) 321.

[4] C. Baktash, B. Haas and W. Nazaerewicz, Annu. Rev. Nucl. Part. Sci. 45 (1995) 485.

[5] C. Baktash, Prog. Part. Nucl. Phys. 38 (1997) 291.

[6] J. Dobaczewski, Proc. Int. Conf. on Nuclear Structure '98 (AIP conference proceedings 481), ed. C. Baktash, p. 315.

[7] R.K. Sheline, I. Ragnarsson and S.G. Nilsson, Phys. Lett. B 41 (1972) 115.

[8] G. Leander and S.E. Larsson, Nucl. Phys. A 239 (1975) 93.

[9] I. Ragnarsson, S.G. Nilsson and R.K. Sheline, Phys. Rep. 45 (1978) 1.

[10] T. Bengtsson, M.E. Faber, G. Leander, P. Möller, M. Ploszajczak, I Ragnarsson and S. Åberg, Phys. Scr. 24 (1981) 200.

[11] M. Girod and B. Grammaticos, Phys. Rev. C 27 (1983) 2317.

[12] H. Molique, J. Dobaczewski, J. Dudek, Phys. Rev. C 61 (2000) 044304.

[13] R.R. Rodriguez-Guzmán, J.L. Egido and L.M. Robeldo, Phys. Rev. C 62 (2000) 054308.

[14] T. Tanaka, R.G. Nazmitdinov and K. Iwasawa, Phys. Rev. C 63 (2001) 034309.

[15] A.V. Afanasjev, P. Ring and I. Ragnarsson, in:D. Rudolph, M. Hellström (Eds.), Proc. Int. Workshop on Selected Topics on N=Z Nuclei (PINGST 2000), Lund, Sweden, June 6-10, 2000, p.183.

[16] C.E. Svenson *et al.*, Phys. Rev. Lett. 85 (2000) 2693.

[17] C.E. Svenson *et al.*, Phys. Rev. C 63 (2001) 061301(R).

[18] C.E. Svenson *et al.*, Nucl. Phys. A 682 (2001) 1c.

[19] E. Ideguchi *et al.*, Phys. Rev. Lett. **87** (2001), 222501.

[20] C.D. O'Leary, M.A. Bentley, B.A. Brown, D.E. Appelbe, R.A. Bark, D.M. Cullen, S. Ertürk, A. Maj and A.C. Merchant, Phys. Rev. C 61 (2000) 064314.

[21] M. Yamagami and K. Matsuyanagi, Nucl. Phys. **A672** (2000), 123.

[22] K.T.R. Davies, H. Flocard, S.J. Krieger and M.S. Weiss, Nucl. Phys. A 342 (1980) 111.

[23] H. Flocard, P.H. Heenen, S.J. Krieger and M.S. Weiss, Nucl. Phys. A 391 (1982) 285.

[24] H. Flocard, P.H. Heenen, S.J. Krieger and M.S. Weiss, Prog. Theor. Phys. 72 (1984) 1000.

[25] P. Bonche, H. Flocard, P.H. Heenen, S.J. Krieger and M.S. Weiss, Nucl. Phys. A 443 (1985) 39.

[26] P. Bonche, H. Flocard, P.H. Heenen, Nucl. Phys. A 467 (1987) 115.

[27] N. Tajima, S. Takahara and N. Onishi, Nucl. Phys. A 603 (1996) 23.

[28] N. Tajima, Prog. Theor. Phys. Supple. No. 142 (2001) 265.

[29] S. Takahara, N. Tajima and N. Onishi, Nucl. Phys. A 642 (1998) 461.

[30] S. Takami, K. Yabana and K. Ikeda, Prog. Theor. Phys. 96 (1996) 407.

[31] S. Takami, K. Yabana and M. Matsuo, Phys. Lett. B 431 (1998) 242.

[32] P.-G. Reinhard, D.J. Dean, W. Nazarewicz, J. Dobaczewski, J.A. Maruhn and M.R. Strayer, Phys. Rev. C 60 (1999) 014316.

[33] M. Bender and P.-H. Heenen, to be published in Rev. Mod. Phys.

[34] J. Dechargé and D. Gogny, Phys. Rev. C 21 (1980) 1568.

[35] P. Ring, Prog. Part. Nucl. Phys. 37 (1996) 193.

[36] S. Frauendorf, Rev. Mod. Phys. 73 (2001) 463.

[37] M. Yamagami, K. Matsuyanagi and M. Matsuo, Proc. Int. Workshop on Selected Topics on N=Z Nuclei (PINGST 2000), Lund, Sweden, June 6-10, 2000, p.76.

[38] T. Inakura, M. Yamagami, S. Mizutori and K. Matsuyanagi, Proc. Yukawa Int. Seminar on Physics of Unstable Nuclei (YKIS01) (Prog. Theor. Phys. Supple.), Kyoto, Japan, Nov. 5-10, 2001, in press.

[39] H. Flocard, P. Quentin, A.K. Kerman and D. Vautherin, Nucl. Phys. A 203 (1973) 433.

[40] D. Baye and P.-H. Heenen, J. Phys. A 19 (1986) 2041.

[41] M. Beiner, H. Flocard, Nguyen van Giai and P. Quentin, Nucl. Phys. A 238 (1975) 29.

[42] J. Bartel, P. Quentin, M. Brack, C. Guet and H.-B. Håkansson, Nucl. Phys. A 386 (1982) 79.

[43] E. Chabanat, P. Bonche, P. Haensel, J. Meyer and F. Schaeffer, Nucl. Phys. A 635 (1998) 231.

[44] Gui-Lu Long and Yang Sun, Phys. Rev. C 63 (2001) 021305(R).

[45] W.J. Gerace and A.M. Green, Nucl. Phys. A 93 (1967) 110, *ibid* A 123 (1969) 241.

[46] V. Metag, R. Repnow, P. von Brentano, F. Dickmann and K. Dietrich, Phys. Lett. B 34 (1971) 257.

[47] W.J. Gerace and J.P. Mestre, Nucl. Phys. A 285 (1977) 253.

[48] D.C. Zheng, D. Berdichevsky and L. Zamik, Phys. Rev. C 38 (1988) 437.

[49] D.C. Zheng, L. Zamik and D. Berdichevsky, Phys. Rev. C 42 (1990) 1004.

[50] Y. Kanada-En'yo, nucl-th/0204040, Proc. Yukawa Int. Seminar on Physics of Unstable Nuclei (YKIS01) (Prog. Theor. Phys. Supple.), Kyoto, Japan, Nov. 5-10, 2001, in press .

[51] E. Caurier, F. Nowacki, A. Poves and A. Zuker, nucl-th/0205036.

[52] J.J. Simpson, W.R. Dixon and R.S. Storey, Phys. Rev. Lett. 31 (1973) 946.

[53] F. Michel, S. Ohkubo and G. Reidemeister, Prog. Theor. Phys. Supple. No. 132 (1998) 7.

[54] W.D.M. Rae and A.C. Merchant, Phys. Lett. B 279 (1992) 207.

[55] J. Zhang, W.D.M. Rae and A.C. Merchant, Nucl. Phys. A 575 (1994) 61.

[56] M. Yamagami and K. Matsuyanagi and M. Matsuo, Nucl. Phys. **A693** (2001), 579.

[57] J. Negele, Nucl. Phys. A502 (1989) 371c.

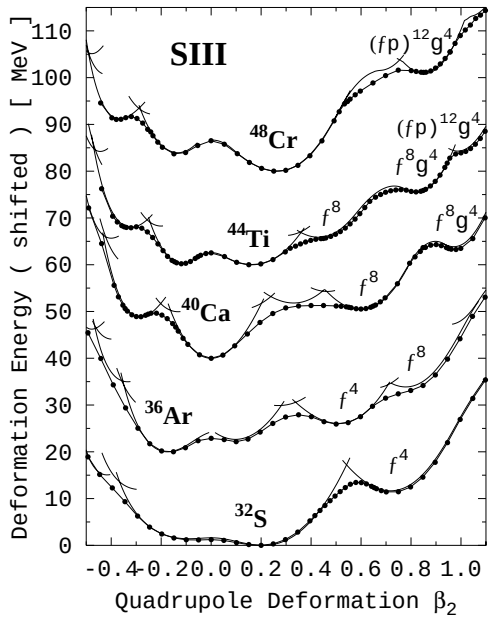

Figure 1: Deformation energy curves as functions of the quadrupole deformation β_2 calculated at $I = 0$ by means of the constrained SHF procedure with the SIII interaction. The axial-asymmetry parameter γ is constrained to be zero. The curves for different nuclei are shifted by 20 MeV to accommodate them in a single plot. Solid lines with and without filled circles represent the results obtained by the unrestricted and restricted versions, respectively (see the text). The notations $f^n g^m$ and $(fp)^n g^m$ indicate the configurations in which the $f_{7/2}$ shell (fp shell) and the $g_{9/2}$ shell are respectively occupied by n and m nucleons.

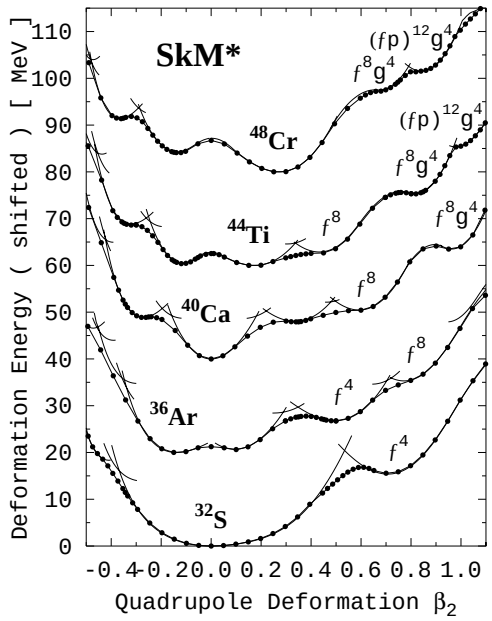

Figure 2: The same as Fig.1 but for the SkM* interaction.

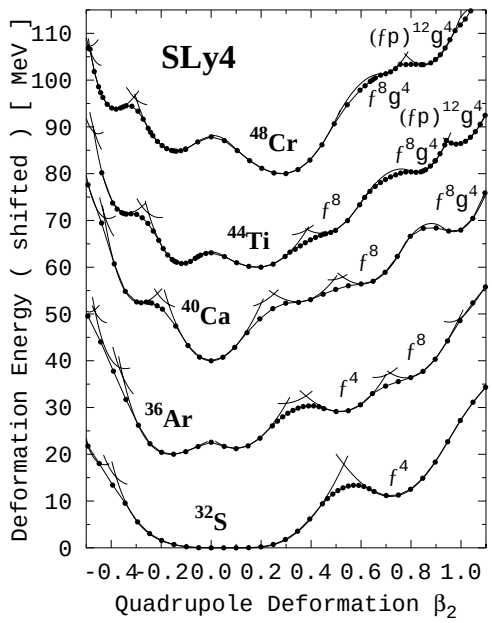

Figure 3: The same as Fig.1 but for the SLy4 interaction.

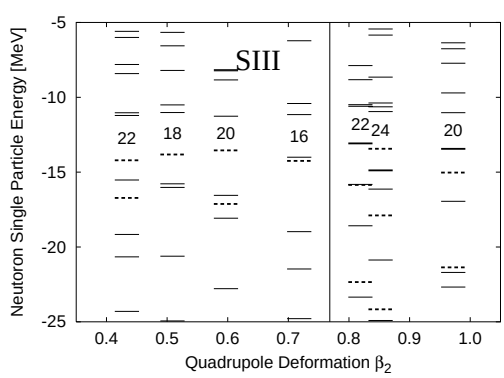

Figure 4: Single-particle energy spectra for neutrons at various SD and HD local minima, calculated at $I = 0$ with the SIII interaction. For every local minima, levels are drawn at positions corresponding to their equilibrium values of β_2. The levels are occupied up to the Fermi levels; on top of them, neutron numbers of the system are indicated. The levels associated with the $f_{7/2}$ and $g_{9/2}$ shells are drawn by broken and thick solid lines, respectively. Single-particle spectra for protons are almost the same as those for neutrons.

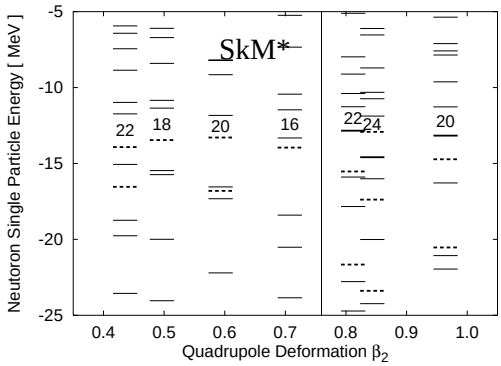

Figure 5: The same as Fig.4 but for the SkM* interaction.

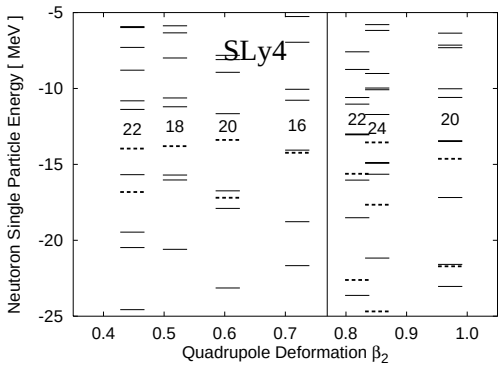

Figure 6: The same as Fig.4 but for the SLy4 interaction.

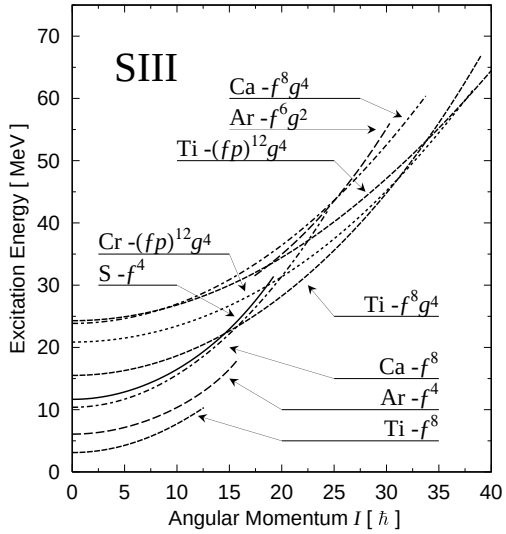

Figure 7: Excitation energy vs. angular-momentum plot for the SD and HD rotational bands obtained by the cranked SHF calculations with the use of the SIII interaction. Their configurations are indicated by the same notations as in Fig. 1.

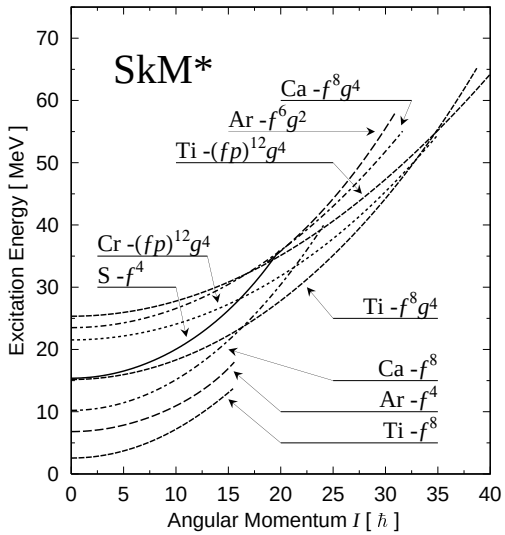

Figure 8: The same as Fig.7 but for the SkM* interaction.

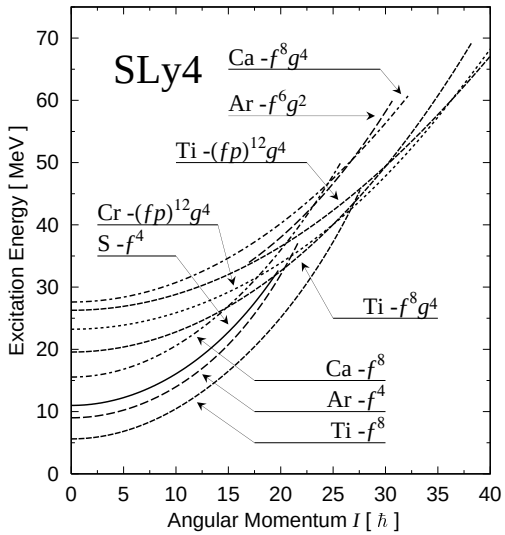

Figure 9: The same as Fig.7 but for the SLy4 interaction.

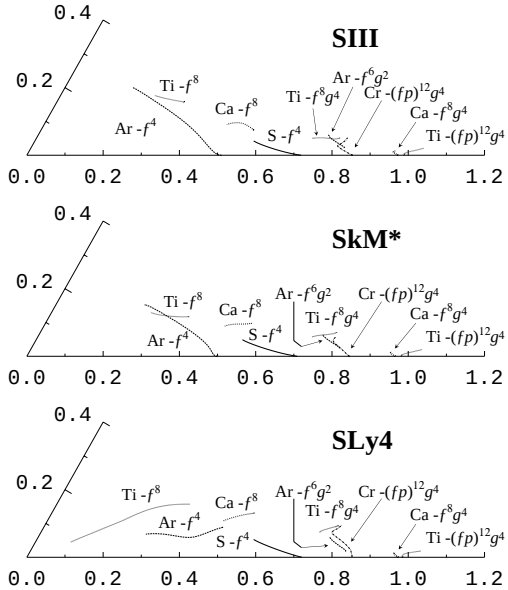

Figure 10: Quadrupole deformation parameters (β_2, γ) and their variations for the SD and HD rotational bands in ^{32}S, ^{36}Ar, ^{40}Ca, ^{44}Ti and ^{48}Cr. The top, middle and bottom panels show the shape evolution in the (β_2, γ) plane, evaluated with the use of the SIII, SkM*, and SLy4 interactions, respectively. Notations and ranges of I for individual bands are the same as those shown in Figs. 7-9. Values of β_2 decrease with increasing I, except for the $(fp)^{12}g^4$ configuration in ^{44}Ti (where β_2 increases with increasing I).

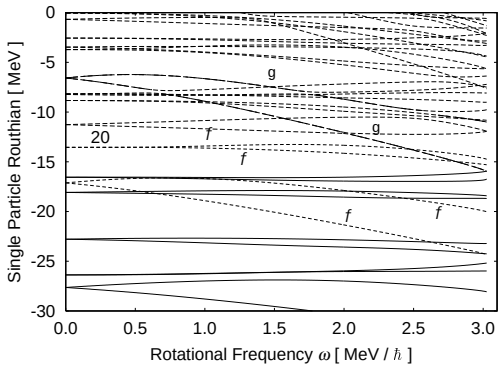

Figure 11: Neutron single-particle energy diagram (Routhian) for the SD band in ^{40}Ca, calculated with the use of the SIII interaction and plotted as functions of rotational frequency $\omega_{\rm rot}$. The levels associated with the $f_{7/2}$ and $g_{9/2}$ shells are drawn by thick-broken and long-dashed lines, respectively.

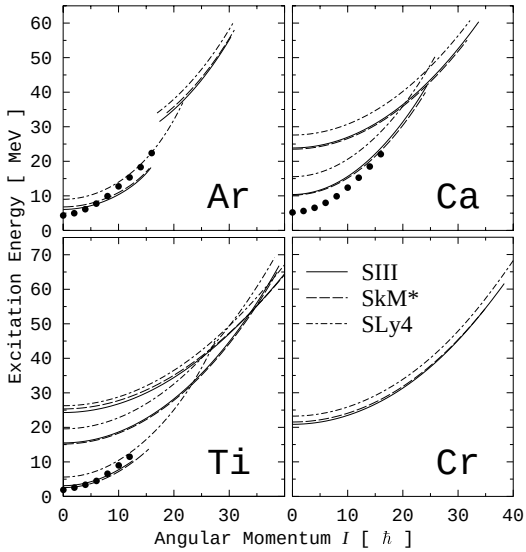

Figure 12: Comparison between the excitation energies of the SD and HD bands in ^{36}Ar, ^{40}Ca, ^{44}Ti and ^{48}Cr, calculated by using different versions of the Skyrme interaction and the experimental data ([16] for ^{36}Ar, [19] for ^{40}Ca, and [20] for ^{44}Ti). The data are shown by filled circles and the results with the SIII, SkM* and SLy4 interactions are drawn by solid, dashed and dashed-dotted lines, respectively.

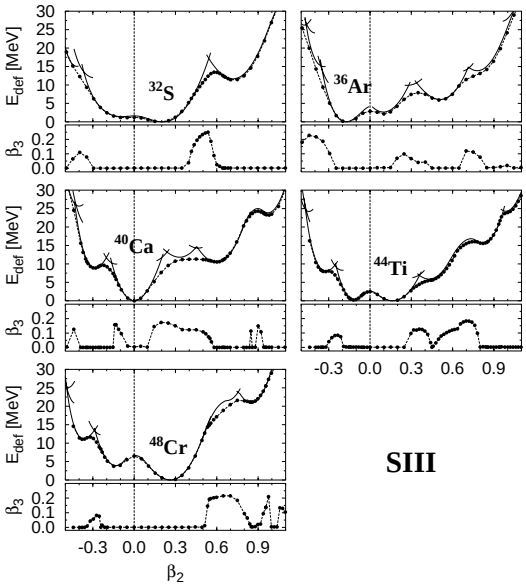

Figure 13: Octupole deformation paramaters β_3 of the lowest energy states for given values of β_2, obtained by the unrestricted SHF calculation at $I = 0$ with the use of the SIII interaction. Their values are plotted as functions of β_2 in the lower portion of each panel. To show that their values increase at crossing regions between configurations involving different number of particles in the fp shell, the deformation energy curves are also displayed in the upper portion of each panel. The latter are the same as those presented in Fig. 1.

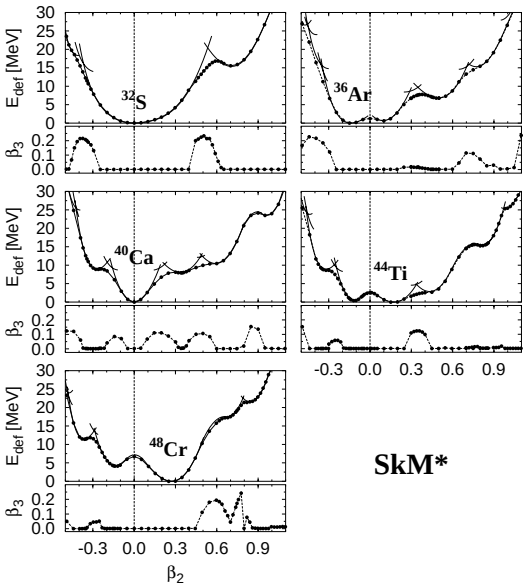

Figure 14: The same as Fig.13 but for the SkM* interaction.

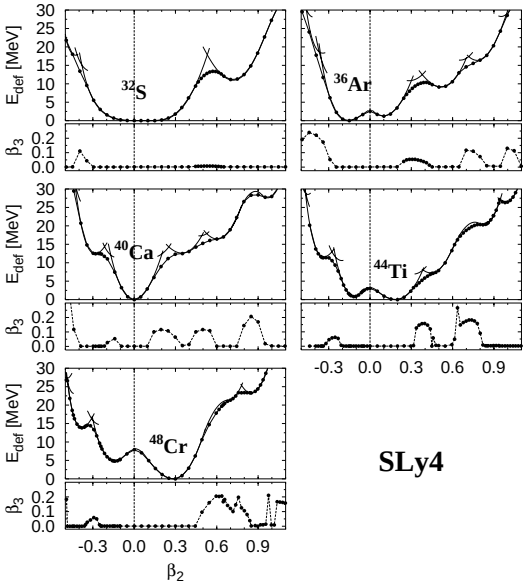

Figure 15: The same as Fig.13 but for the SLy4 interaction.

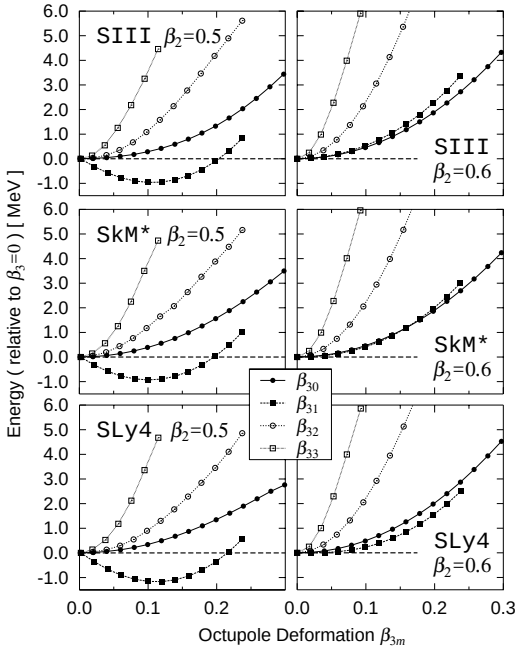

Figure 16: Left-hand side: Deformation energy curves (measured from energies at $\beta_3 = 0$) as functions of the octupole deformation parameters $\beta_{3m}(m = 0, 1, 2, 3)$, calculated for ^{40}Ca by means of the constrained HF procedure. The quadrupole deformation parameters are fixed at $\beta_2 = 0.5$ and $\gamma = 0$. One of the $\beta_{3m}(m = 0, 1, 2, 3)$ is varied while the other β_{3m}'s are fixed to zero. Right-hand side: The same as the left-hand side, except that the quadrupole deformation parameters are fixed at $\beta_2 = 0.6$ and $\gamma = 0$. Results of calculation with the use of the SIII, SkM*, and SLy4 interactions are displayed in the upper, middle and lower panels, respectively.